Original Article

Wall Shear Stress Estimation for 4D Flow MRI Using Navier–Stokes Equation Correction

Jiacheng Zhang,[1] Sean M. Rothenberger,[2] Melissa C. Brindise,[3] Michael Markl,[4,5] Vitaliy L. Rayz,[1,2] and Pavlos P. Vlachos [1,2]

[1]School of Mechanical Engineering, Purdue University, West Lafayette, IN 47907, USA; [2]Weldon School of Biomedical Engineering, Purdue University, West Lafayette, IN 47907, USA; [3]Department of Mechanical Engineering, Pennsylvania State University, University Park, PA 16802, USA; [4]Feinberg School of Medicine, Northwestern University, Chicago, IL 60611, USA; and [5]McCormick School of Engineering, Northwestern University, Evanston, IL 60208, USA

Associate Editor Umberto Morbiducci oversaw the review of this article.

Abstract—This study introduces a novel wall shear stress (WSS) estimation method for 4D flow MRI. The method improves the WSS accuracy by using the reconstructed pressure gradient and the flow-physics constraints to correct velocity gradient estimation. The method was tested on synthetic 4D flow data of analytical Womersley flow and flow in cerebral aneurysms and applied to *in vivo* 4D flow data acquired in cerebral aneurysms and aortas. The proposed method's performance was compared to the state-of-the-art method based on smooth-spline fitting of velocity profile and the WSS calculated from uncorrected velocity gradient. The proposed method improved the WSS accuracy by as much as 100% for the Womersley flow and reduced the underestimation of mean WSS by 39 to 50% for the synthetic aneurysmal flow. The predicted mean WSS from the *in vivo* aneurysmal data using the proposed method was 31 to 50% higher than the other methods. The predicted aortic WSS using the proposed method was 3 to 6 times higher than the other methods and was consistent with previous CFD studies and the results from recently developed methods that take into account the limited spatial resolution of 4D flow MRI. The proposed method improves the accuracy of WSS estimation from 4D flow MRI, which can help predict blood vessel remodeling and progression of cardiovascular diseases.

INTRODUCTION

Vascular wall shear stress (WSS) is an important determinant of endothelial function and phenotype.[24] WSS has emerged as an essential feature of atherogenesis.[10,15] The low WSS due to disturbed blood flow promotes atherogenesis,[10,11] while high WSS is associated with plaque rupture.[17] Abnormal WSS is also related to the growth and rupture of intracranial aneurysms.[6,9,21,27] Additionally, WSS and WSS-derived metrics such as oscillatory shear index (OSI) are correlated with aortopathy. The distribution of low WSS and high OSI resembles the regions of aortic atherosclerotic lesions,[16,25] and the abnormal WSS in the bicuspid aortic valve (BAV) patients was associated with the aortic dilation.[1,2,42] Therefore, the information on the magnitude, distribution, and variation of WSS can provide valuable insights for predicting and assessing vascular diseases.

WSS can be estimated from the velocity gradient at the vascular wall. 4D flow magnetic resonance imaging (MRI) resolves blood flow in space and time *in vivo*, enabling the estimation of WSS.[26,40] Stalder *et al.*[39] introduced a method to evaluate the aortic WSS from the B-spline interpolation of the 4D flow velocity on manually positioned 2D planes. However, this method only resolves the WSS on the 2D slices, and the plane selection can be laborious. Several methods were introduced later to resolve the 3D WSS distribution on the vessel wall from the velocity profile along the wall-normal direction at each wall point.[4,5,33] The method proposed by Potters *et al.*[33] uses smooth spline fitting

Address correspondence to Pavlos P. Vlachos, School of Mechanical Engineering, Purdue University, West Lafayette, IN 47907, USA. Electronic mail: pvlachos@purdue.edu

of the velocity along the wall-normal direction and assumes no-slip boundary condition to evaluate the velocity gradients and WSS. The method has been applied to 4D flow data acquired in the aorta,[42,33] carotid arteries,[12,33] and intracranial aneurysms.[43]

The accuracy of the WSS estimated from 4D flow data is affected by the spatial resolution and segmentation.[12,31,33] A significant inverse relationship was found between the estimated WSS and the spatial resolution of 4D flow data.[12] The WSS estimated from *in vivo* 4D flow MRI was inconsistent with the results from high-resolution modalities, including computational fluid dynamics (CFD) and *in vitro* particle imaging velocimetry (PIV), potentially due to the limited resolution of MRI. The aortic WSS estimated from *in vivo* 4D flow data was 0–2 Pa,[2,42,39] while patient-specific CFD models yielded a range of 0–30 Pa.[22,32,34] The WSS estimated from 4D flow MRI was also lower than the CFD results in intracranial aneurysms and carotid bifurcations, and the differences were more significant in regions of higher WSS.[41] Several multi-modality studies showed that the mean WSS evaluated from *in vivo* 4D flow MRI in the intracranial aneurysms was less than half of the results from patient-specific CFD simulations and *in vitro* PIV measurements.[7,43] Because of the discrepancy in WSS magnitudes, the normalized parameters such as the normalized WSS and OSI are usually preferred for clinical and physiological investigations as they possess qualitatively similar distributions between MRI and other modalities.[7,31,41]

This study aims to introduce a method to enhance the WSS estimation with 4D flow MRI. The proposed method, termed pressure-gradient induced velocity-gradient correction (PG-VGC), corrects the velocity gradient based on the reconstructed pressure field gradient to improve the estimated WSS's accuracy. The conservation laws of mass and linear momentum are incorporated to formulate a linear system. This linear system is used to estimate the velocity-gradient errors with a least-squares approach. The error is then subtracted from the velocity gradient to improve the assessment of WSS. The method was first tested with synthetic 4D flow data of Womersley flow and flow in two cerebral aneurysms. The method was then applied to *in vivo* 4D flow data acquired in the cerebral aneurysms and aortas.

MATERIALS AND METHODS

Wall Shear Stress Estimation with Navier–Stokes Equation Correction

The WSS vector $\vec{\tau}$ can be calculated as:

$$\vec{\tau} = 2\mu\bar{\bar{\varepsilon}} \cdot \vec{n}, \tag{1}$$

where μ is the dynamic viscosity of the blood, $\vec{n}$ is the inward wall-normal vector with a magnitude of 1, and $\bar{\bar{\varepsilon}}$ is the deformation or strain rate tensor. The WSS value represents the magnitude of $\vec{\tau}$ in this study, and the time-averaged WSS (TAWSS) denotes the WSS averaged arithmetically over a cardiac cycle. The deformation tensor can be expressed as:

$$\bar{\bar{\varepsilon}} = \frac{1}{2}\left(\overline{\overline{\nabla u}} + \left(\overline{\overline{\nabla u}}\right)^{\mathrm{T}}\right), \tag{2}$$

where $\overline{\overline{\nabla u}}$ is the velocity gradient tensor which can be determined from the velocity field of the blood flow using numerical differentiation or interpolation.[4,5,33]

Figure 1a presents the proposed WSS estimation procedure with PG-VGC. The velocity gradient and the pressure field are first calculated from the 4D flow data. The spatial gradient of the pressure field is employed to correct the velocity gradient based on the conservation of mass (COM) and conservation of linear momentum (COLM). The WSS is then determined from the corrected velocity-gradient. Figure 1b demonstrates that PG-VGC uses the data in the whole region with blood flow (ROI) for estimating WSS. The ROI consists of the voxels within the lumen and the partial volume voxels whose centers locate inside the surfaces representing the vessel wall. The details of the algorithm are provided as follows:

Pressure Reconstruction with Wall-Distance-Based Weighted Least-Squares

The wall points where the WSS is of interest and the center points of the 4D flow voxels within the blood flow are combined to a list of N spatial points. The instantaneous pressure gradients at these spatial points were estimated from the velocity field based on the COLM[46] as:

$$\nabla_i p = -\rho\left(\frac{\partial \boldsymbol{u_i}}{\partial t} + \boldsymbol{u} \circ G_x\boldsymbol{u_i} + \boldsymbol{v} \circ G_y\boldsymbol{u_i} + \boldsymbol{w} \circ G_z\boldsymbol{u_i}\right) + \mu\nabla^2\boldsymbol{u_i}, \tag{3}$$

where the subscript $i \in \{x, y, z\}$ indicates the spatial dimension. $\nabla_i p$ is the column vector ($\in \mathbb{R}^N$) of the pressure-gradient along each dimension at the spatial points. $\boldsymbol{u_x} \equiv \boldsymbol{u}$, $\boldsymbol{u_y} \equiv \boldsymbol{v}$, and $\boldsymbol{u_z} \equiv \boldsymbol{w}$ represent the column vectors ($\in \mathbb{R}^N$) of the velocity component along each encoded direction. $\circ$ represents the Hadamard (elementwise) product, and ρ is the fluid density. The temporal derivatives of velocity were calculated using the second order central (SOC) difference scheme. G_x, G_y, and G_z are the discrete gradient operators (matrices) with a size of $N \times N$. The coefficients in the
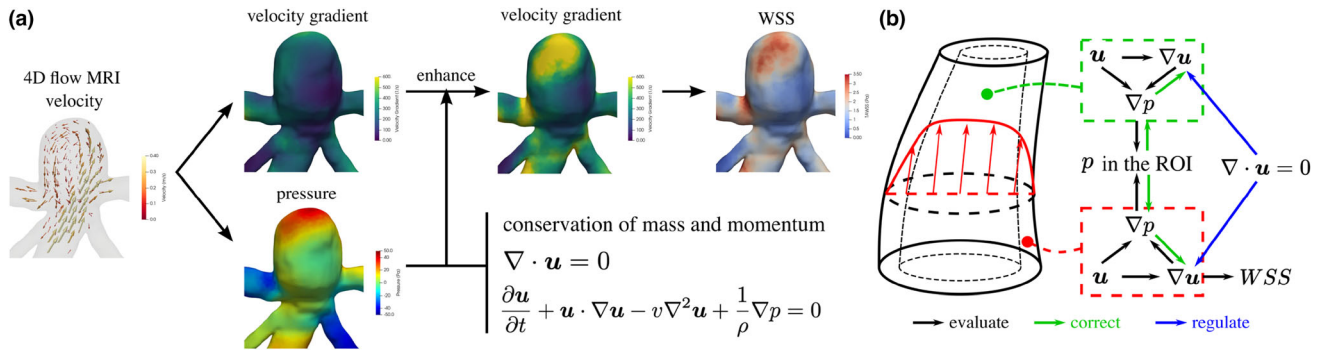
FIGURE 1. (a) The flow chart of the WSS estimation procedure with PG-VGC method. (b) The schematic demonstrates that the flow data in the whole region of interest (ROI) is used for enhancing the WSS estimation. The ROI consists of the voxels within the lumen and the partial volume voxels whose centers locate inside the surfaces representing the vessel wall. The green box and red box indicate the data in the core-flow and near-wall regions, respectively.

operators were determined using the RBF-generated finite difference method (RBF-FD),[45] which is a meshless computational method based on the localized RBF-interpolant in a compact finite-difference mode. The RBF-FD method approximates the function derivative at the center node x_1 as the linear combination of the function values $u(x_k)$ at n support nodes $x_k \in \mathbb{R}^3$ for $k = 1, \dot{s}, n$ as:

$$\mathcal{L}u(x_1) \approx \sum_{k=1}^{n} w_{1,k}u(x_i), \tag{4}$$

where $\mathcal{L}$ denotes the derivative operator, e.g., the gradient along a spatial dimension, and $w_{1,k}$ with $k = 1, \dot{s}, n$ is the RBF-FD weights determined by solving the linear system[19]:

$$\begin{bmatrix} \Phi & e \\ e^{\mathrm{T}} & 0 \end{bmatrix} \begin{bmatrix} w \\ \mu \end{bmatrix} = \begin{bmatrix} \mathcal{L}\phi_1 \\ 0 \end{bmatrix}, \tag{5}$$

with $\Phi_{k,l} = \phi(\|x_l - x_k\|)$ for $k, l = 1, \dot{s}, n$

where $\phi(\|\cdot\|)$ is the RBF function, e is a column vector consisting of ones with a size of n, $\mathcal{L}\phi_1 = [\mathcal{L}\phi(\|x_1 - x_1\|) \quad \cdots \quad \mathcal{L}\phi(\|x_1 - x_n\|)]^{\mathrm{T}}$ is a column vector of the derivative values of the RBF, and μ is the constant that enforces the zero summation of the RBF-FD weights. In this study, the multi-quadratic RBF is used and expressed as:

$$\phi(r) = \sqrt{\frac{r^2}{c^2} + 1}, \tag{6}$$

where $c > 0$ is the shape parameter of the RBF. The support nodes are selected as the spatial points within 2 times of the diagonal length of the 4D flow voxel from the center node x_1 including itself, and the shape parameter c is determined as the mean of the distances from the support nodes to the center node. Each row of the discrete gradient operators G_x, G_y, and G_z consists of the RBF-FD weights determined from (5)

for each spatial point, and the discrete gradient operator transforms the function values to the corresponding gradient values, e.g.,

$$\nabla_x u \approx G_x u. \tag{7}$$

The discrete Laplacian operator was generated from the gradient operators as:

$$\nabla^2 = G_x G_x + G_y G_y + G_z G_z. \tag{8}$$

The pressure field in the whole ROI was reconstructed by spatially integrating the pressure gradients with weighted least-squares (WLS)[46] as:

$$p_{\mathrm{WLS}} = p\mathrm{argmin}(\|\mathcal{W}(Gp - \nabla p)\|), \tag{9}$$

with $G = \begin{bmatrix} G_x \\ G_y \\ G_z \end{bmatrix}$ and $\nabla p = \begin{bmatrix} \nabla_x p \\ \nabla_y p \\ \nabla_z p \end{bmatrix}$, where $p_{\mathrm{WLS}} \in \mathbb{R}^N$ is the column vector containing the reconstructed pressure at the spatial points, $\|\cdot\|$ represents the L2 norm, and the weight matrix $\mathcal{W}$ is a diagonal matrix with a size of $3N \times 3N$. Each diagonal element of $\mathcal{W}$ corresponds to a spatial point and controls the influence of the pressure gradients at the point on the resulting pressure field. The weight was specified as:

$$w_{\mathrm{diag}} = (w_{\max} - w_{\min})\frac{s}{s_{\max}} + w_{\min}, \tag{10}$$

with $w_{\min} = 1$ and $w_{\max} = 10$,

where $w_{\mathrm{diag}} > 0$ is the diagonal element, s is the distance from the corresponding point to its closest wall point, $s_{\max}$ is the maximum s in the ROI and corresponds to the radius of the largest artery in the ROI, and $w_{\min}$ and $w_{\max}$ are the minimum and maximum weights, respectively. Equation (10) specifies the weights to increase linearly with the increase of the distance from the wall, therefore amplifying the effect of the core-flow pressure-gradient on the reconstructed

pressure. It should be noted that the exact values of $w_{\min}$ and $w_{\max}$ do not affect the pressure result if the ratio $w_{\max}/w_{\min}$ remains constant. The solution of Eq. (9) can be obtained by solving the following matrix equation:

$$G^{\mathrm{T}} \mathcal{W}^2 G p_{\mathbf{WLS}} = G^{\mathrm{T}} \mathcal{W}^2 \nabla p, \qquad (11)$$

which is similar to the equation solved for the least-squares reconstruction in the previous work[20] with an additional weight matrix. In the present study, the pressure field is directly solved from Eq. (9) using LSQR, an iterative method for solving sparse least-squares problems,[29,30,37] which is implemented in Python using the "scipy.sparse.linalg.lsqr" function. At least one reference point is required for determining the pressure field from the pressure gradients. In this study, the reference point is selected as an arbitrary point in the blood flow region with a reference pressure of 0 Pa. The selection of the reference point and the reference pressure should not affect the velocity-gradient correction in the later steps as only the spatial gradient of the reconstructed pressure field is used.

Pressure-Gradient-Induced Velocity-Gradient Correction

The velocity gradient ($\overline{\overline{\nabla u}}$) evaluated from 4D flow data can be decomposed into a true component ($\overline{\overline{\nabla u}}_{\mathrm{true}}$) and an error component ($\overline{\overline{\nabla u}}_{\mathrm{err}}$) as:

$$\overline{\overline{\nabla u}} = \overline{\overline{\nabla u}}_{\mathrm{true}} + \overline{\overline{\nabla u}}_{\mathrm{err}}. \qquad (12)$$

$\overline{\overline{\nabla u}}_{\mathrm{err}}$ arises from the velocity measurement errors and gradient calculation. The COLM and COM can be expressed with the velocity gradient tensor as:

$$\frac{\partial \bar{u}}{\partial t} + \partial \bar{u} \cdot \overline{\overline{\nabla u}} - v \nabla \cdot \overline{\overline{\nabla u}} + \frac{1}{\rho} \nabla p = 0, \qquad (13)$$

$$\nabla \cdot \bar{u} \equiv \frac{\partial u}{\partial x} + \frac{\partial v}{\partial y} + \frac{\partial w}{\partial z} = \overline{\overline{I}} : \overline{\overline{\nabla u}} = 0, \qquad (14)$$

where $\partial \bar{u} = [u \quad v \quad w]^{\mathbf{T}}$ is the flow velocity vector, p is the pressure, ∇ represents the gradient operator, "$\nabla \cdot$" represents the divergence operator, and $v = \frac{\mu}{\rho}$ is the kinematic viscosity. $\overline{\overline{I}}_{ij} = \delta_{ij}$ is the identity tensor, and "$:$" is the double dot product such that $\overline{\overline{I}} : \overline{\overline{\nabla u}} = \delta_{ij} \overline{\overline{\nabla u}}_{ij}$. The left-hand-side of (13) and (14) can be nonzero because of $\overline{\overline{\nabla u}}_{\mathrm{err}}$ and the errors in $\partial \bar{u}$ and ∇p. Assuming that $\overline{\overline{\nabla u}}_{\mathrm{err}}$ is the major source of error, the equalities of (13) and (14) can be achieved by replacing $\overline{\overline{\nabla u}}$ with $\overline{\overline{\nabla u}}_{\mathrm{true}}$, and the following equations can be subsequently derived from (13) and (14) by substituting $\overline{\overline{\nabla u}}_{\mathrm{true}}$ for $\overline{\overline{\nabla u}} - \overline{\overline{\nabla u}}_{\mathrm{err}}$ according to (12) as:

$$\left(\bar{u} - v\nabla \right) \cdot \overline{\overline{\nabla u}}_{\mathrm{err}} = \frac{\partial \bar{u}}{\partial t} + \partial \bar{u} \cdot \overline{\overline{\nabla u}} - v\nabla \cdot \overline{\overline{\nabla u}} + \frac{1}{\rho} \nabla p, \qquad (15)$$

$$\overline{\overline{I}} : \overline{\overline{\nabla u}}_{\mathrm{err}} = \overline{\overline{I}} : \overline{\overline{\nabla u}}. \qquad (16)$$

Equations (15) and (16) relate $\overline{\overline{\nabla u}}_{\mathrm{err}}$ to the residuals of (13) and (14), respectively, and can be used to estimate $\overline{\overline{\nabla u}}_{\mathrm{err}}$.

With the reconstructed pressure $p_{\mathbf{WLS}}$, the following linear system can be constructed based on (10):

$$\begin{bmatrix} \boldsymbol{u} - vG_x & \boldsymbol{v} - vG_y & \boldsymbol{w} - vG_z \end{bmatrix} \begin{bmatrix} \nabla_x \boldsymbol{u}_{\mathbf{i,err}} \\ \nabla_y \boldsymbol{u}_{\mathbf{i,err}} \\ \nabla_z \boldsymbol{u}_{\mathbf{i,err}} \end{bmatrix}$$

$$= \frac{\partial \boldsymbol{u}_i}{\partial t} + \boldsymbol{u} \circ G_x \boldsymbol{u}_i + \boldsymbol{v} \circ G_y \boldsymbol{u}_i + \boldsymbol{w} \circ G_z \boldsymbol{u}_i - v\nabla^2 \boldsymbol{u}_i$$
$$+ \frac{1}{\rho} G_i p_{\mathbf{WLS}}, \qquad (17)$$

where the subscript $i \in \{x, y, z\}$ indicates the spatial dimension. $\nabla_x \boldsymbol{u}_{\mathbf{i,err}} \in \mathbb{R}^N$ is the column vector containing the errors in $\frac{\partial u_i}{\partial x}$, and this convention also applies to other velocity-gradient error terms. $G_i p_{\mathbf{WLS}}$ is the spatial gradient of the reconstructed pressure. Three linear systems can be constructed from (17) for the COLM along x, y, and z dimensions. A linear system for the COM can be formulated based on (16) as:

$$\begin{bmatrix} I & I & I \end{bmatrix} \begin{bmatrix} \nabla_x \boldsymbol{u}_{\mathbf{err}} \\ \nabla_y \boldsymbol{v}_{\mathbf{err}} \\ \nabla_z \boldsymbol{w}_{\mathbf{err}} \end{bmatrix} = G_x \boldsymbol{u}_x + G_y \boldsymbol{u}_y + G_z \boldsymbol{u}_z, \qquad (18)$$

where I represents the identity matrix with a size of $N \times N$. The linear systems of (17) and (18) were combined to form a linear system with 4N equations and 9N unknown velocity-gradient errors. The combined linear system is underdetermined with infinite number of solutions as there are fewer equations than unknowns. The linear system was also solved with the LSQR method implemented in Python which provides the solution with the least L2 norm. The velocity gradients initially evaluated using the discrete gradient operators were corrected by subtracting the estimated velocity gradient errors, e.g.,

$$\nabla_x \boldsymbol{u}_{\mathbf{corr}} = G_x \boldsymbol{u} - \nabla_x \boldsymbol{u}_{\mathbf{err}}, \qquad (19)$$

And the WSS was determined from the corrected velocity-gradient according to (1) and (2).

Since the velocity gradient also affects the reliability of the pressure reconstruction, we have implemented an iterative procedure that uses the corrected velocity-gradient for the pressure reconstruction and the

BMES BIOMEDICAL ENGINEERING SOCIETY

velocity-gradient correction in the next iteration. The flowchart in Fig. 2 demonstrates the iterative algorithm. The convergence of the WSS is determined based on the relative root-mean-square (RMS) change of WSS defined as:

$$\Delta(\text{WSS}) = \|\text{WSS}_{ct} - \text{WSS}_{ct-1}\| / \|\text{WSS}_{ct-1}\|, \quad (20)$$

where $\Delta(\text{WSS})$ is the relative RMS change of WSS, WSS_{ct} represents the WSS obtained from the iteration ct, and $\| \cdot \|$ represents the L2 norm. The WSS is considered to be converged if $\Delta(\text{WSS}) < 0.01$, and the maximum number of iterations is 5.
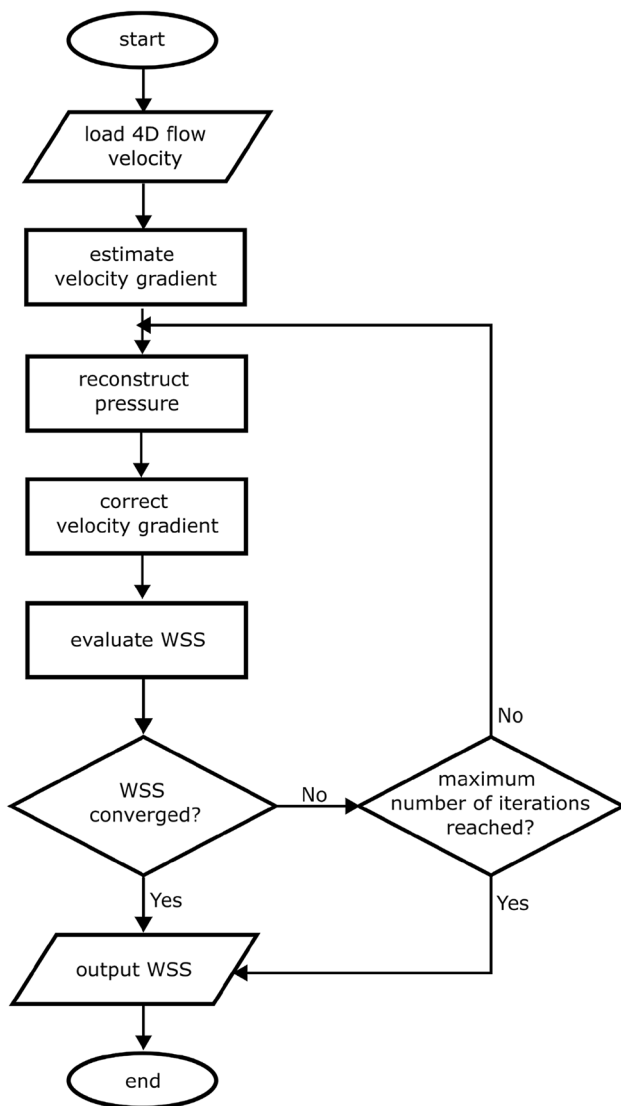

FIGURE 2. The iterative procedure of PG-VGC. The corrected velocity-gradient is used for the pressure reconstruction and velocity-gradient correction in the next iteration.

Aneurysmal Flow Acquisition and Simulation

To test the proposed PG-VGC method with real arterial flows, *in vivo* 4D flow MRI data were acquired in a basilar tip (BT) aneurysm at San Francisco VA Medical Center and an internal carotid artery (ICA) aneurysm at Northwestern Memorial Hospital with a 3T MRI scanner (Skyra, Siemens Healthcare, Erlangen, Germany). The 4D flow data were on Cartesian grids with the spatial resolution of $1.25 \times 1.25 \times 1.33 \text{mm}^3$ for the BT aneurysm and $1.09 \times 1.09 \times 1.30 \text{mm}^3$ for the ICA aneurysm. The temporal resolution was 40.5 ms (20 frames per cycle) and 44.8 ms (13 frames per cycle) for the BT and ICA aneurysms, respectively. The contrast-enhanced magnetic resonance angiography (CE-MRA) data was also acquired for the BT aneurysm with the spatial resolution of $0.7 \times 0.7 \times 0.7 \text{mm}^3$. For the ICA aneurysm, non-contrast time of flight (TOF) angiography was acquired with a spatial resolution of $0.4 \times 0.4 \times 0.6 \text{mm}^3$. The CE-MRA and TOF images were segmented to create surfaces (STL) of the vessel wall. The 4D flow data were registered to and masked by the STL geometries. To ensure the smoothness of the aneurysmal geometry, the STL surfaces were processed with Laplacian smoothing which moves each vertex to the averaged location of its neighboring vertices on the surface. The wall points and wall-normal extracted from the STL surfaces were used for evaluating and analyzing the WSS. Approval of all ethical procedures and protocols was granted by the Institutional Review Boards (IRB) at Purdue University, Northwestern Memorial Hospital, and San Francisco VA Medical Center.

Additionally, CFD simulations were performed using FLUENT 18.1 (ANSYS) with the created STL surfaces and the flow waveforms obtained from 4D flow data as the inflow and outflow boundary conditions. The flow was assumed to be laminar, incompressible, and Newtonian. The walls of the vessel were assumed to be rigid. The density and dynamic viscosity used for the simulations were 1060kg/m^3 and 0.0035Pas. More details on the *in vivo* imaging and CFD simulations can be found in Ref. [7].

In Vivo Aortic 4D Flow MRI Acquisition

In vivo 4D flow data were acquired in the aortas from three subjects to evaluate the performance of PG-VGC, including a patient with BAV, a patient with tricuspid aortic valve and an aortic aneurysm (TAV-AA), and a health control subject with tricuspid aortic valve. The scans were performed in a sagittal oblique volume on a 1.5 T scanner (MAGNETOM Avanto, Aera, Siemens, Erlangen, Germany) at Northwestern Memorial Hospital with prospective ECG gating and

during free breathing. Gadolinium-based contrast (Magnevist, Ablavar, or Gadavist) were used for imaging the two patients, while no contrast was used on the control subject. The resolutions and scan parameters were presented in Table 1. The v_{enc} was 150 cm/s for the TAV-AA and control scans and 175 cm/s for the BAV scan. No velocity aliasing was observed. The patient data for this IRB approved study were retrospectively included with waiver of consent. The healthy control subject underwent a research cardiac MRI after written informed consent was obtained from the study participant. A static mask of the blood vessel was created for each dataset based on the magnitude image and the time-averaged velocity magnitude, which was manually corrected by an expert observer using Mimics (Materialise NV, Belgium). A smooth surface (STL) was then generated from the mask with Laplacian smoothing to represent the vessel walls. The wall points and wall-normal from the surfaces were used for estimating the WSS.

Performance Evaluation and WSS Error Analysis Method

The proposed method's performance was first evaluated on synthetic 4D flow datasets of the analytical Womersley flow with varying Womersley number and spatial resolution as given in the supplementary material, and the WSS from the analytical solution was employed as the "ground truth". Additionally, the method was tested on synthetic 4D flow datasets created based on the velocity fields from the CFD simulations of the cerebral aneurysms with the same spatial and temporal resolutions as the *in vivo* acquisition and a velocity-to-noise ratio (VNR) of 10%, and the WSS from the CFD was considered as the "ground truth".

The WSS error level of each test case was represented by the RMS error (RMSE) evaluated as:

$$\text{RMSE} = \sqrt{\frac{\sum_{i=1}^{N_t} \sum_{j=1}^{N_{wall}} \left(\text{WSS}_{i,j} - \text{WSS}_{\text{true},i,j} \right)^2}{N_t \times N_{wall}}}, \quad (21)$$

where N_t and N_{wall} represent the number of timeframes and the number of wall points, respectively. The relative RMSE was determined as the RMSE normalized by the RMS of the ground truth WSS.

To demonstrate the improvement by PG-VGC, the state-of-the-art method introduced by Potters *et al.*[33] was employed in this study and referred to as "Spline" since it evaluates the WSS with the smooth-spline fitting of the velocity profile. WSS was also estimated using (1) and (2) from the uncorrected velocity gradients and was referred to as "Vgrads". The accuracy of Spline and Vgrads was also assessed and compared to the PG-VGC method. For the aortic flow data, we also used the two surrogate methods introduced by Corso *et al.*[14] to estimate the WSS and compare to the PG-VGC method. The methods determine the WSS based on the maximum coordinate invariant Reynolds shear stress (RSS_{max}) and the maximum coordinate invariant viscous shear stress (VSS_{max}) at a normalized distance of $\sim\Delta$ from the wall as:

$$\text{WSS}_{\text{M1}}^* = \rho^* C \frac{\tilde{\Delta}}{2R^*} \text{VSS}_{\text{max},\tilde{\Delta}}, \quad (22)$$

$$\text{WSS}_{\text{M2}}^* = \rho^* K \frac{\tilde{\Delta}}{2} \sqrt{\text{RSS}_{\text{max},\tilde{\Delta}}} \text{VSS}_{\text{max},\tilde{\Delta}} Re, \quad (23)$$

where WSS_{M1}^* and WSS_{M2}^* are the nondimensionalized WSS estimated using method 1 (M1) and method 2 (M2), respectively. ρ^* denotes the relative density, and the reference length and velocity for the nondimensionalization are the inlet radius and twice the mean inflow velocity. The nondimensional constants C and K are optimized through regressions with direct numerical simulation (DNS) data of aortic flow[14].

RESULTS

Error Analysis with Synthetic 4D Flow Data

Figure 3a presents the normalized streamwise velocity profile and the velocity gradient with respect to radius (dw/dr) at the peak flow rate from the analytical solutions of the Womersley flow with different Womersley number (α). With an increase of α, the shear layer became thinner leading to a steeper velocity gradient near the wall. Figure 3b shows the time-dependent median of the streamwise pressure gradient

TABLE 1. The spatial and temporal resolutions, the number of cardiac timeframes (N_{time}), the flip angle, echo time (T_E), and repetition time (T_R) for the *in vivo* aortic scans

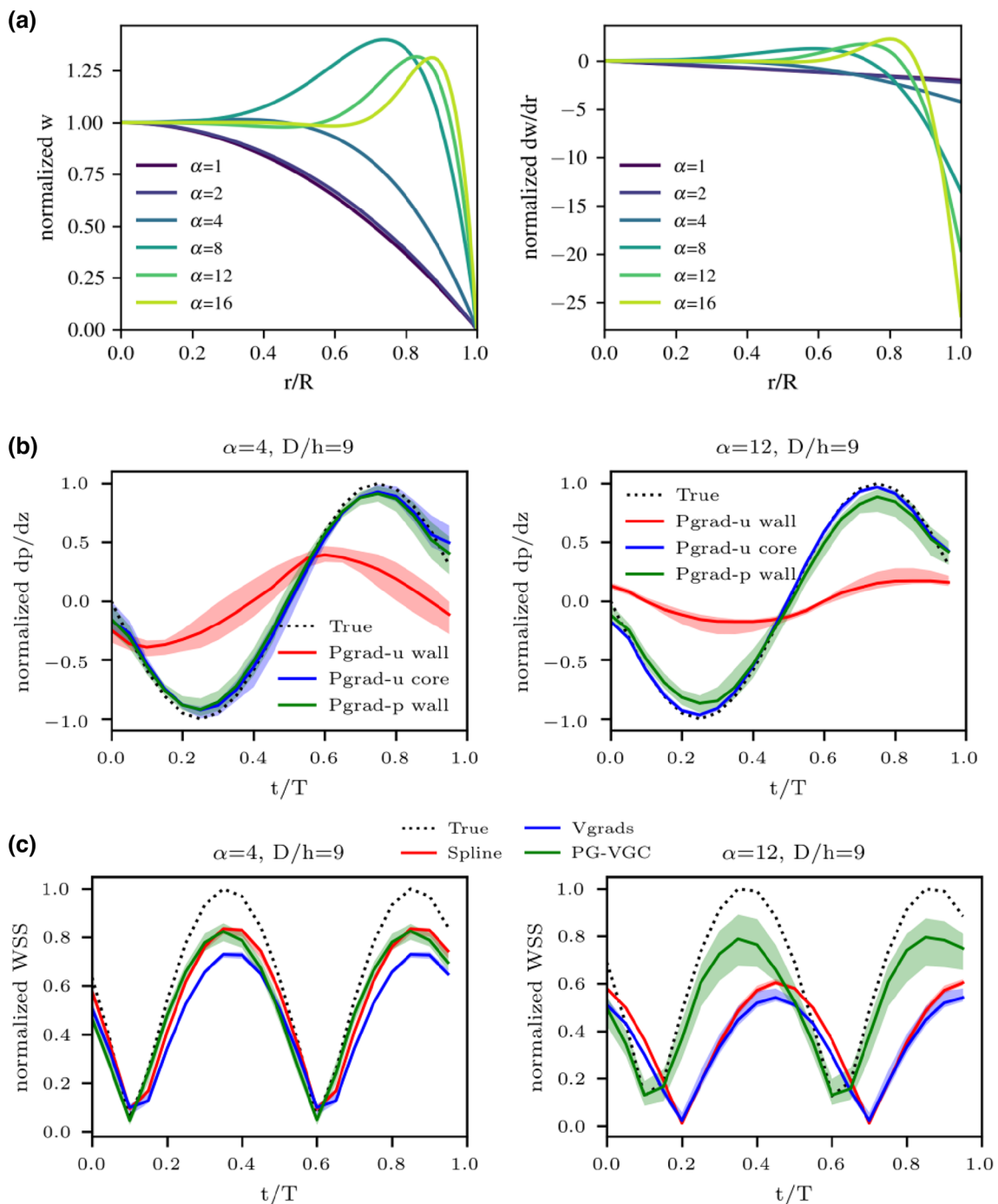| Subject	Voxel size (mm³)	Δt(ms)	N_{time}	Flip angle (°)	T_E/T_R (ms)
TAV-AA	2.375 × 2.375 × 3	37.6	21	15	2.3/4.7
BAV	2.125 × 2.125 × 2.5	38.4	24	15	2.4/4.8
Control	2.375 × 2.375 × 2.4	38.4	21	7	2.5/4.8

FIGURE 3. (a) The streamwise velocity and velocity gradient profiles for Womersley flow with different Womersley numbers (α). The velocity is normalized by the centerline velocity (w_{center}), and the velocity gradient is normalized by w_{center}/R. (b) The time-dependent median and interquartile range (IQR) of the streamwise pressure-gradient estimated at the wall points and in the core-flow region. Pgrad-u denotes the pressure gradient evaluated from the local velocity data, and Pgrad-p indicates the gradient of the reconstructed pressure field. The pressure gradients were normalized by the amplitude of the streamwise pressure-gradient from the analytical solution. (c) The time-dependent median and IQR of the WSS estimated from different methods in one flow cycle.

($\mathrm{d}p/\mathrm{d}z$) estimated from the flow data with α of 4 and 12 and a spatial resolution of $D/9$. The pressure gradient directly evaluated from velocity field with (3) is denoted as "Pgrad-u", while "Pgrad-p" represents the gradient of the reconstructed pressure field. The legends "wall" and "core" indicate the pressure gradient at the wall points and in the core-flow region with $r < 0.5R$, respectively. For both datasets, the Pgrad-u in the core-flow matched the true $\mathrm{d}p/\mathrm{d}z$ with errors less than 0.1 for most timeframes, while the Pgrad-u at the

wall deviated from the true solution by as much as 0.5 for $\alpha = 4$ and up to 0.8 for $\alpha = 12$. The Pgrad-p at the wall achieved similar accuracy as the Pgrad-u in the core-flow and was more reliable than the Pgrad-u at the wall. Figure 3c compares the WSS estimated using different methods with the "ground truth" from the analytical solution, and the WSS was normalized by the amplitude of the true WSS. The Spline and PG-VGC methods estimated similar WSS results at $\alpha = 4$ and were more accurate than the estimation by Vgrads. With $\alpha = 12$, Spline and Vgrads underestimated the WSS amplitude by 40% with a phase shift of approximately 0.1 s, while PG-VGC underestimated the WSS amplitude by 20%.

Figure 4 presents the relative RMSE of the estimated WSS from the synthetic Womersley flow datasets with different α, grid resolution, and noise level. The cases with a grid resolution less than 0.5 mm or greater than 3.5 mm were uncommon in practical applications and were excluded from the analysis. The wedge area corresponds to the relative RMSE of each method, and the color on the wedge indicates the RMSE by Spline or Vgrads as compared to PG-VGC. A red wedge suggests higher RMSE by Spline or Vgrads than PG-VGC, while a blue wedge indicates that the WSS estimated by Spline or Vgrads were more accurate than PG-VGC. The proposed PG-VGC method yielded more accurate WSS for most datasets than Spline and Vgrads. Greater improvement was achieved by PG-VGC for higher α with more than 100% improvement at α of 12 and 16. The estimated WSS's accuracy was affected by the resolution and α. The 10% noise led to slightly increased RMSE for several cases with relatively fine resolution as compared to the results without noise.

Synthetic and In Vivo Aneurysmal 4D Flow

The velocity fields at peak systole from the CFD simulations, the synthetic 4D flow data, and the *in vivo* 4D flow data were shown in Fig. 5 for the BT and ICA aneurysms. For the BT aneurysm, the flow entered from the basilar artery, circulated in the aneurysmal sac, and then exited primarily through the posterior cerebral arteries (PCAs). For the ICA aneurysm, the flow entered from the ICA, circulated in the aneurysmal sac, and exited through the distal ICA and the middle cerebral artery (MCA).

The Bland–Altman plots in Fig. 6a compare the CFD WSS with the WSS estimated by Spline, Vgrads, and PG-VGC from the synthetic aneurysmal data. The mean WSS from CFD was 2.1 and 1.9 Pa for the BT aneurysm and ICA aneurysm, respectively, while the mean WSS was underpredicted by 0.57 to 1.23 Pa by the three methods as presented in Fig. 6a. The PG-VGC method reduced the WSS underestimation by 39 to 50% and improved the robustness compared to the other methods, as suggested by the lower bias values and standard deviations. Figure 6b compares the spatial distributions of the TAWSS from CFD and synthetic MRI. High WSS regions were observed in the anterior view and superior view of the BT aneurysmal sac in CFD results, which PG-VGC also predicted, but absent in the results obtained by Spline and Vgrads. For the ICA aneurysm, the PG-VGC method predicted the high WSS region at the tip of the aneurysmal sac from the superior view, which was missing from Spline and Vgrads results. Moreover, PG-VGC yielded higher WSS in the ICA than Spline and Vgrads, which was more consistent with CFD. The time-dependent median and interquartile range (IQR) of the WSS distributions are provided in Fig. 6c. The estimated WSS waveforms using the three methods have similar
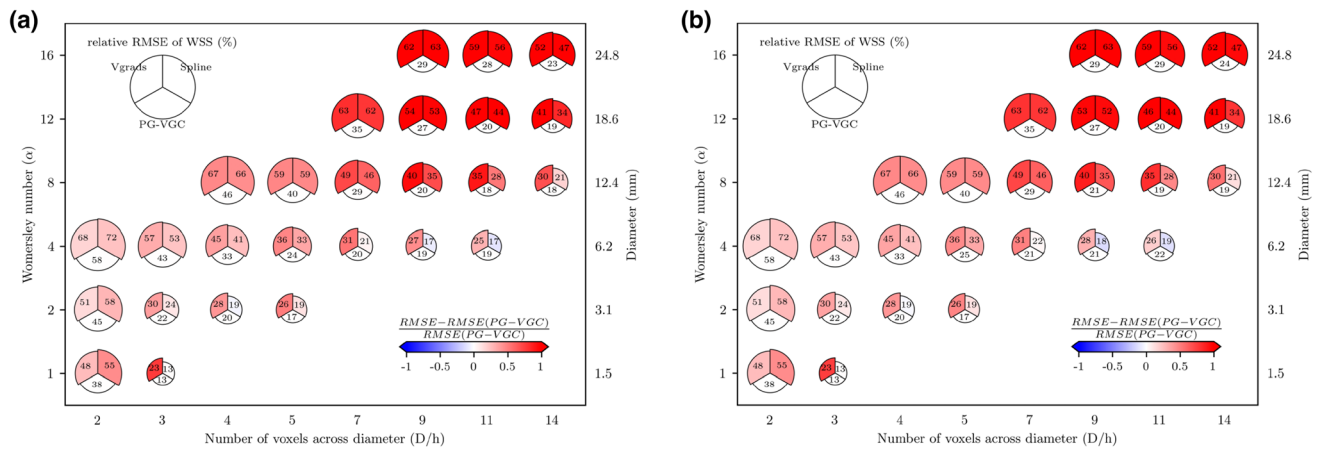

FIGURE 4. The relative RMSE of WSS estimated from synthetic Womersley 4D flow datasets with 0% noise (a) and 10% noise (b). The area of each wedge corresponds to the relative RMSE by each method, and the color scale indicates the comparison between the RMSE from Spline or Vgrads with PG-VGC as expressed by the formula over the color bar.
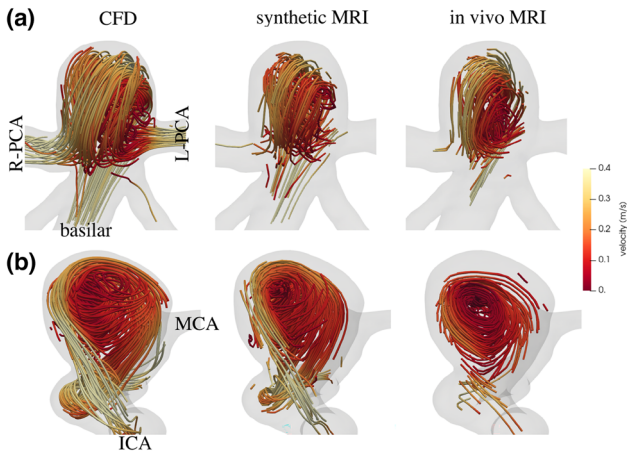
FIGURE 5. The velocity fields at peak systole of the BT (a) and ICA (b) aneurysms from CFD, synthetic MRI, and *in vivo* MRI.

shape with the waveform from CFD despite the differences in the amplitudes. Additionally, the Pearson correlation coefficient between the estimated WSS waveforms and the "ground truth" waveforms from CFD was determined, and the histograms of the correlation coefficients from all the wall points are presented in Fig. 6c. The mean correlation coefficients between the estimated WSS waveforms and the CFD waveforms are greater than 0.8 for all three methods. The waveforms obtained by PG-VGC have slightly higher correlation coefficients than Spline and Vgrads in terms of the mean and median values.

Figure 7a shows the shows the change of the WSS differences between the PG-VGC and the CFD results as a function of the noise level added to the synthetic aneurysmal flow data. Both the mean and the standard deviation of the WSS differences are insensitive to the
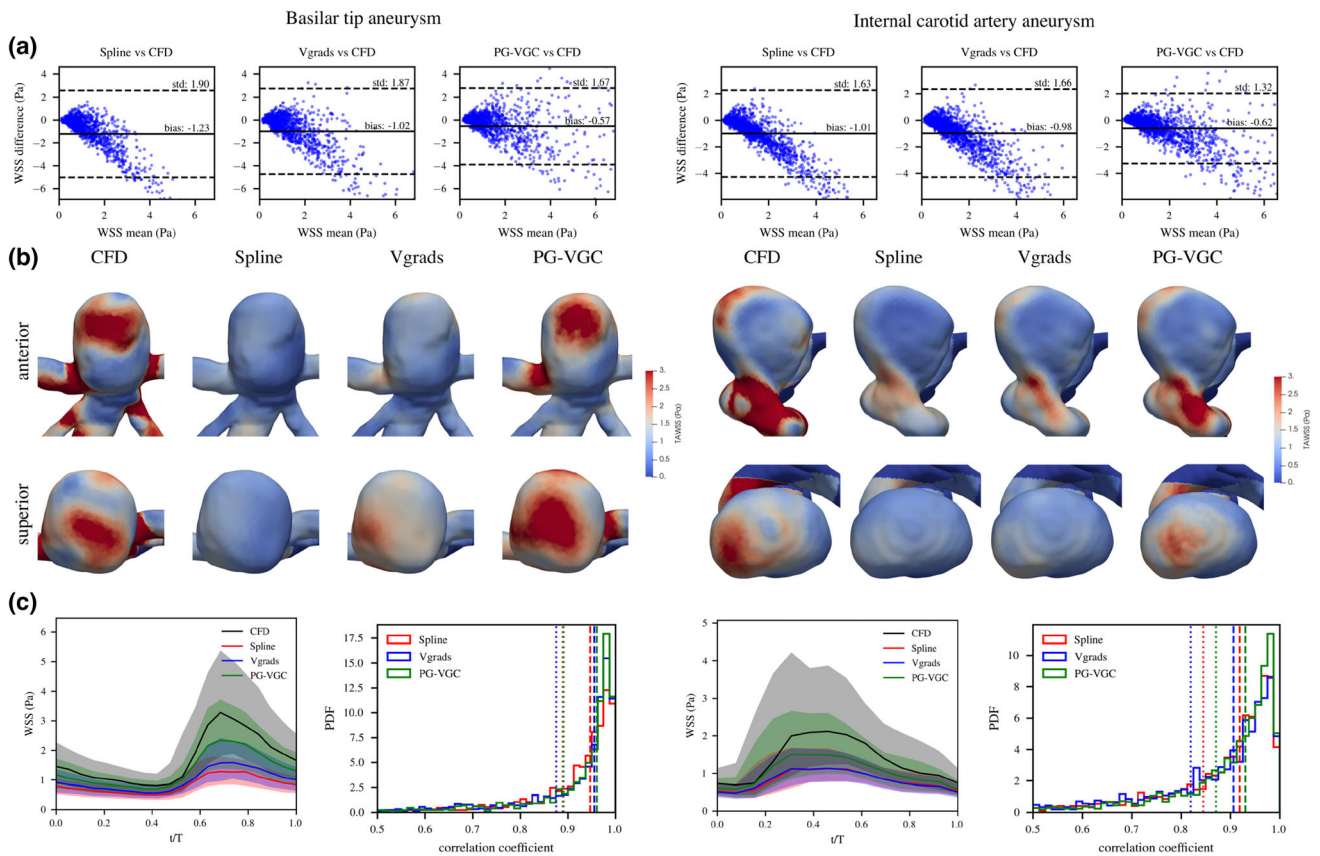

FIGURE 6. (a) The Bland–Altman plots comparing the WSS estimated from synthetic 4D flow data with the WSS from CFD at all cardiac phases, with the mean and standard deviation (std) of the WSS differences presented in the plots. (b) The spatial distributions of the TAWSS estimated from the synthetic 4D flow data and from CFD. (c) The time-dependent median and IQR of the WSS estimated from the aneurysmal flow data in a cardiac cycle, and the probability density distributions of the Pearson correlation coefficients between the estimated WSS waveforms and the CFD waveforms at all the wall points. The dotted vertical lines and the dashed vertical lines represent the mean and the median of the correlation coefficient distributions, respectively.
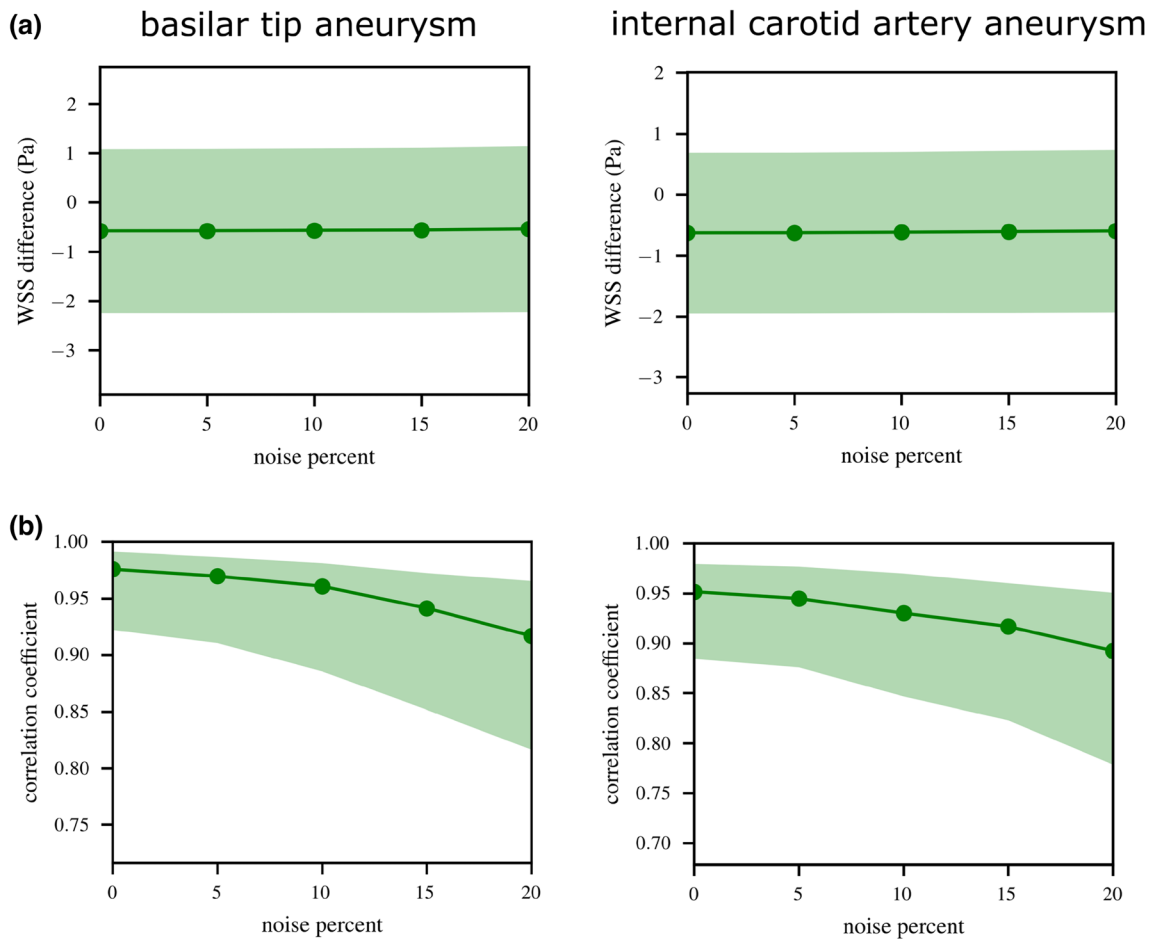
(a)

(b)

FIGURE 7. (a) The change of the WSS difference between the results by PG-VGC and CFD as a function of the noise level of the aneurysmal flow data. The solid line indicates the mean of the WSS differences from all spatiotemporal points, and the bounds of the shaded region are the mean ± the standard deviation of the WSS differences. (b) The distribution of the Pearson correlation coefficient between the WSS waveforms estimated by PG-VGC and CFD as a function of the noise level. The solid line indicates the median correlation coefficients from all the wall points, and the shaded region is bounded by the 25th and 75th percentiles.

level of noise in the flow data. Figure 7b presents the change of the Pearson correlation coefficient between the WSS waveforms estimated by PG-VGC and CFD as a function of the noise level. The median of the correlation coefficients from all the wall points changes from 0.97 to 0.92 for the BT aneurysm and from 0.95 to 0.90 for the ICA aneurysm, suggesting that the accuracy of the estimated WSS waveforms is slighted affected by the noise level in the flow data.

Figure 8a compares the statistical distributions of the TAWSS estimated from the *in vivo* aneurysmal data. The mean TAWSS estimated by Spline was 46 and 33% lower than that estimated by PG-VGC for the BT and ICA aneurysm, respectively, while the mean TAWSS obtained by Vgrads was 31 and 50% lower than that from PG-VGC for the BT and ICA aneurysm respectively. Figure 8b presents the time-dependent median and IQR of the estimated WSS for the two aneurysms. The different methods obtained

similar WSS waveforms; however, PG-VGC predicted higher WSS than the other methods at all timeframes. Figure 8c shows the spatial distributions of the estimated TAWSS. PG-VGC predicted additional high WSS regions in the BT aneurysmal sac as shown on the anterior and superior views. The three methods yielded qualitatively similar TAWSS distributions for the ICA aneurysm, with higher WSS predicted by PG-VGC than the other two methods around the "neck" of the aneurysmal sac.

In Vivo Aortic 4D Flow MRI

Figure 9a compares the statistical distributions of the TAWSS estimated from the *in vivo* aortic data of the three subjects. The mean TAWSS by PG-VGC was 4.4 to 5.4 times the mean TAWSS assessed by Spline and 3.0 to 3.8 times the mean TAWSS assessed by Vgrads. The mean TAWSS by PG-VGC is close to the
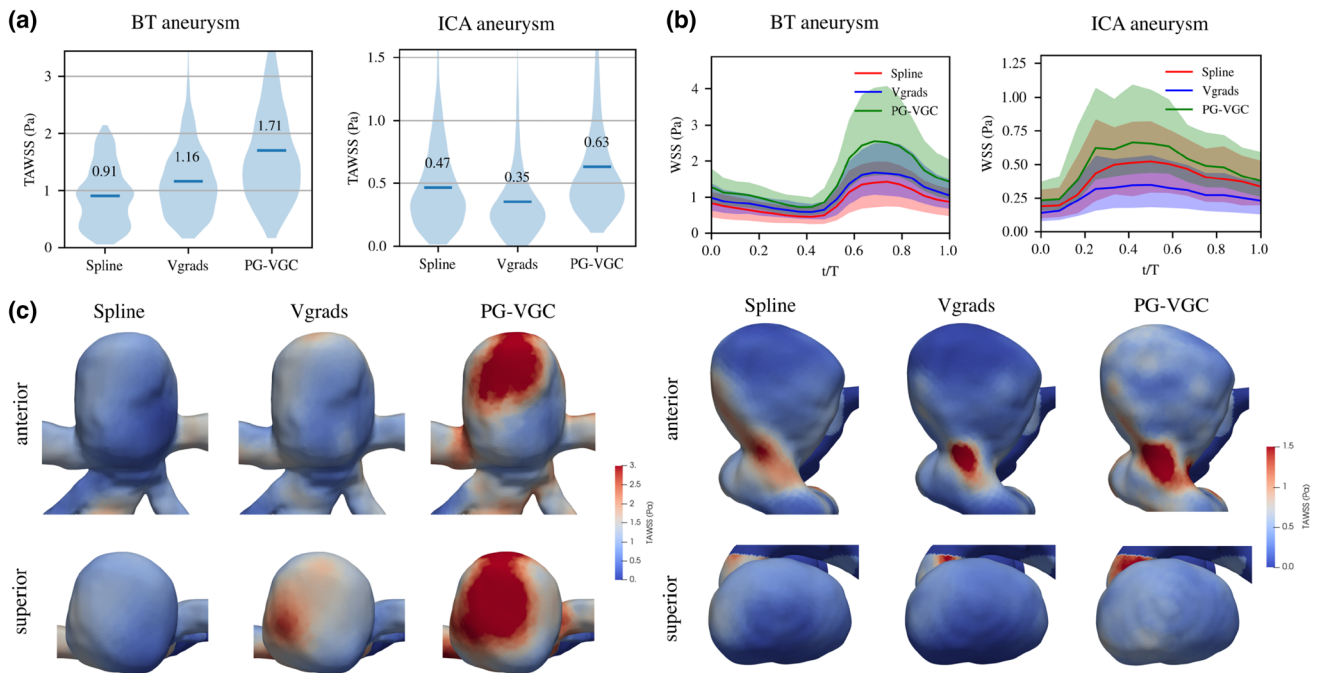
FIGURE 8. (a) The statistical distributions and mean values of the TAWSS estimated from *in vivo* 4D flow data of the BT aneurysm and the ICA aneurysm. (b) The time-dependent median and IQR of the WSS estimated from the *in vivo* 4D flow data in a cardiac cycle. (c) The spatial distributions of the TAWSS estimated from the *in vivo* 4D flow data.

mean TAWSS by M1 and is 30% to 40% lower than the TAWSS by M2. Similar profiles of the time-dependent median of WSS were obtained from all methods as shown in Fig. 9b, while PG-VGC predicted higher WSS and larger IQR for all the timeframes than Spline and Vgrads. The M2 predicted the highest median WSS and IQR among all the methods. The median WSS estimated at peak systole was 1 to 2 Pa by Spline and Vgrads, 4 to 7 Pa by PG-VGC, 4 to 6 Pa by M1, and 7 to 12 Pa by M2.

Figure 10 presents the velocity field, the vortical structure (VS), the pressure distribution on the wall, and the relative WSS at peak systole. The relative WSS is defined as the WSS normalized by its global average at peak systole for the three subjects. The peak-systolic velocity fields are represented using 3D pathlines whose color corresponds to the velocity magnitude. The VSs are included because it has shown to be correlated with high WSS in the aorta.[3] The VSs were detected using the Q-criterion[18] with the velocity gradients evaluated using the SOC scheme from the 4D flow data and are represented by the iso-surfaces in Fig. 10 at peak systole. Both the right-anterior (R-A) and the posterior-left (P-L) views were presented. The green circles in the PG-VGC WSS distributions indicate the high WSS regions predicted by PG-VGC but are absent from the other estimations. For all subjects, VSs were observed in the ascending aorta near the aortic root and in the descending aorta near the aortic

arch, with a corresponding location of the local minimum pressure. For the control subject, high WSS regions around the VSs were calculated by all the methods, as shown on the R-A view. However, only PG-VGC predicted the marked high WSS regions on the P-L view. For the TAV-AA subject, PG-VGC predicted the high WSS region in the aneurysm at the aortic arch, which was missing from the results obtained with other methods. PG-VGC also yielded the high WSS region next to the VS in the ascending aorta near the P-L wall. For the BAV subject, PG-VGC predicted multiple regions with high WSS in the ascending aorta corresponding to the VSs near the R-A and P-L wall, which were not seen in the results by other methods.

DISCUSSION

This study introduced, evaluated, and applied a method for WSS estimation from 4D flow MRI. The proposed method, PG-VGC, improves the WSS estimation by enhancing the near-wall velocity gradients. The near-wall velocity-gradient calculation from 4D flow data is commonly unreliable because of the systematic velocity errors caused by the partial-volume effects and intravoxel phase dispersion.[35,44] Moreover, the velocity gradient near the wall is typically higher than the core-flow region, therefore increasing the bias
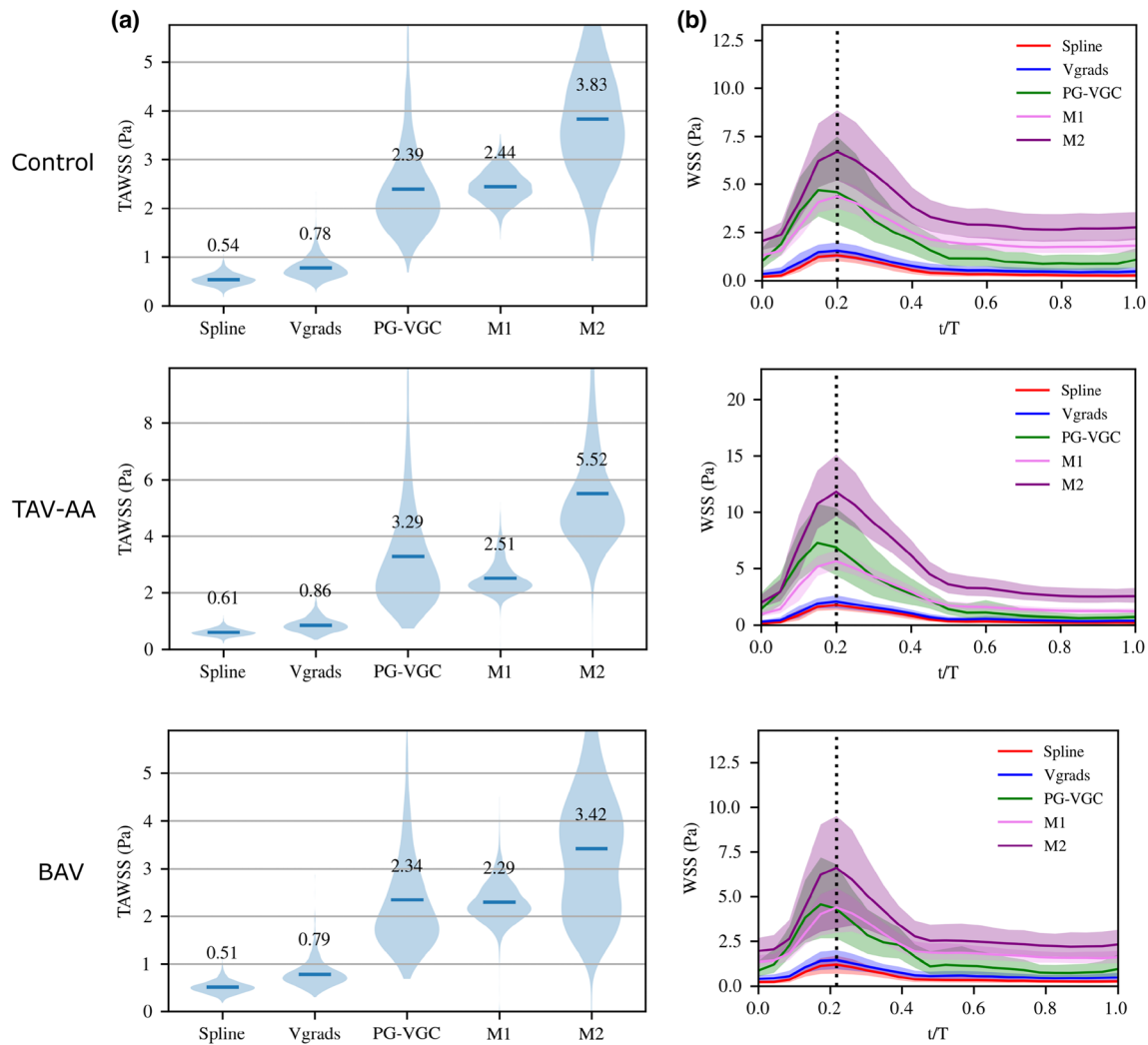
FIGURE 9. (a) The statistical distributions and mean values of the TAWSS estimated from the *in vivo* aortic data. (b) The time-dependent median and IQR of the estimated WSS in the cardiac cycle. The dotted vertical line indicates the phase at peak systole.

error in the gradient calculation in cases with limited spatial resolution. Additionally, the v_{enc} of the 4D flow acquisition is normally significantly higher than the near-wall velocity to avoid velocity aliasing, leading to increased velocity noise which affects the accuracy of the velocity-gradient estimation. The uncertainty in the wall location also affects the velocity-gradient's accuracy if the wall points are incorporated in the gradient evaluation. The velocity-gradient correction by PG-VGC was based on the flow physics constraints of COLM and COM. The divergence-free constraint based on COM has been shown to be effective for denoising and reconstructing the velocity fields acquired with pc-MRI.[8,23,28,36,38,47] At the stationary wall, the COLM is reduced to the balance between the pressure force and the viscous diffusion and directly relates the velocity gradient to the pressure gradient. The near-wall pressure gradient evaluated using (3)

based on the near-wall velocity gradient can be unreliable, while the pressure gradient estimated in the core-flow is more accurate as shown in Fig. 3b. We reconstructed the pressure field in the ROI by spatially integrating the pressure-gradients using WLS. This WLS approach is a global optimization process, dominated by the pressure-gradients in the core-flow regions due to their greater weights. The spatial gradient of the reconstructed pressure in the near-wall region is more reliable than the uncorrected pressure-gradient as shown by comparing Pgrad-u and Pgrad-p in Fig. 3b. Therefore, the more reliable Pgrad-p was used and proved to be effective for correcting the near-wall velocity-gradient.

The PG-VGC method improves the mean and the range of WSS estimated from 4D flow data. A previous study has shown that the WSS estimated in intracranial aneurysms depend on the spatial resolution of the
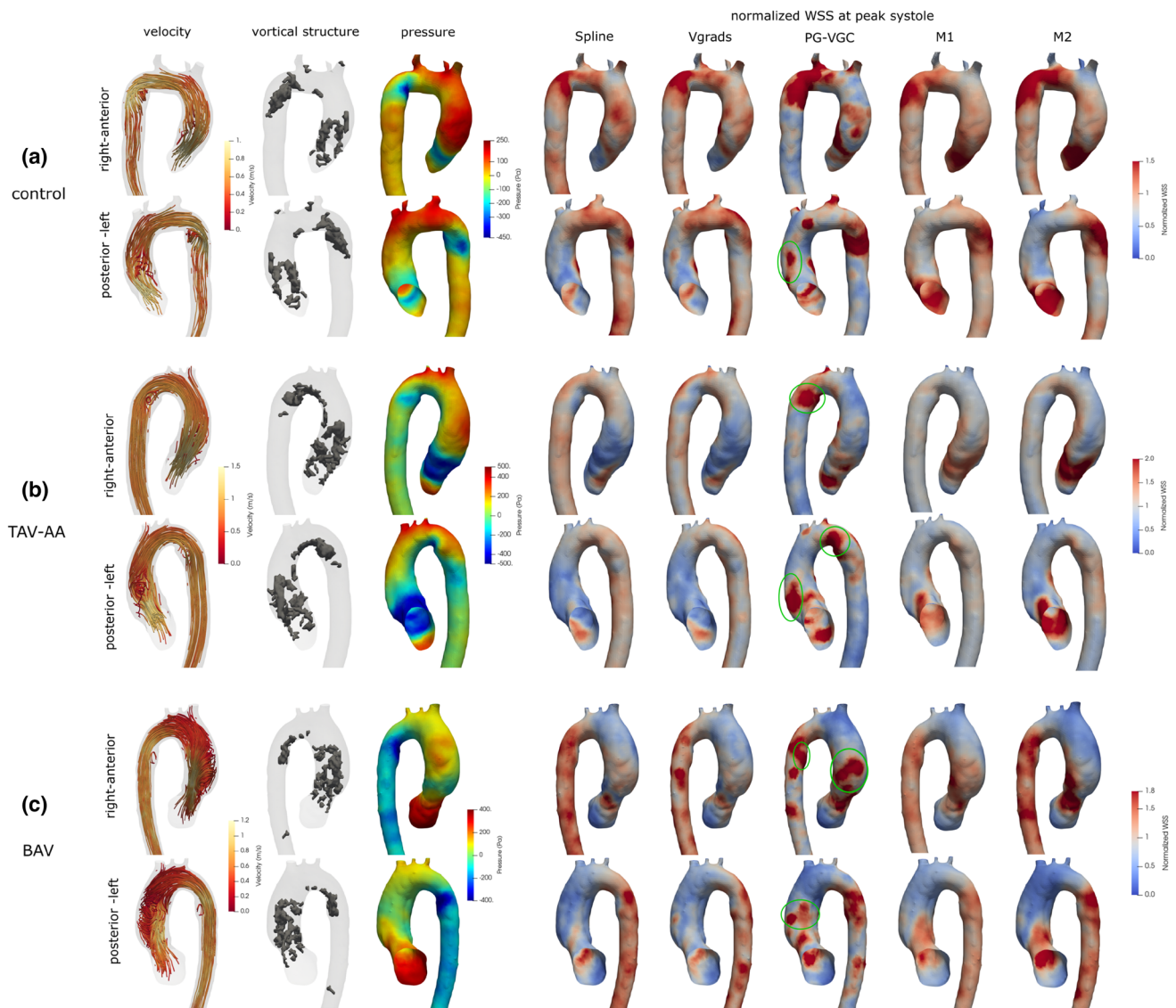
FIGURE 10. The peak-systolic velocity fields represented using 3D pathlines, the vortical structure indicated by iso-surfaces at peak systole, the pressure distribution on the wall at peak systole, and the relative WSS estimated by the Spline, Vgrads, PG-VGC, M1, and M2 methods from the *in vivo* 4D flow data of the control subject (a), the TAV-AA subject (b) and the BAV subject (c) at peak systole. The green circles in the PG-VGC WSS distributions indicate the high WSS regions predicted by PG-VGC but are absent from the other estimations.

phase-contrast MRI data with 50 to 60% underestimation of the mean WSS at a resolution of 1 mm.[43] Therefore, the 31 to 50% increase on the mean WSS prediction by PG-VGC as compared to Spline and Vgrads improved the accuracy of the WSS estimation in the cerebral aneurysms. For the *in vivo* aortic data, Spline and Vgrads yielded a median WSS of 1 to 2 Pa at peak systole, which was consistent with the results in previous studies using similar methods.[2,42,39] However, the common range of mean aortic WSS at peak systole was 5 to 20 Pa according to CFD studies.[22,31,32,34] The underestimation of WSS in the aorta with 4D flow MRI was due to the low spatial resolution of the

imaging data. Perinajová *et al.*[31] estimated the WSS from spatially downsampled CFD data in a flow phantom of aortic coarctation, and the mean WSS was underestimated by 34% at a resolution of 0.2 mm and by 63% at a resolution of 0.7 mm. In the present study, the spatial resolution of *in vivo* aortic MRI data was 2–3 mm, which was expected to cause greater WSS underestimation compared to higher resolutions. PG-VGC predicted 3 to 6 times higher mean WSS than Spline and Vgrads resulting in better agreement with the results from previous CFD studies[22,31,32,34] and the results from two surrogate methods (M1 and M2) based on the velocity gradient tensor and the Reynolds

stress data in proximity of the wall.[14] The overall increase of the WSS magnitude computed by PG-VGC can potentially resolve the inconsistency between the WSS obtained from different modalities as observed in previous studies.[7,43,41] The improvements achieved by PG-VGC method promote the use of WSS in addition to the normalized parameters such as relative WSS and OSI for the investigation of WSS-related cardiovascular diseases with 4D flow MRI.

The PG-VGC method also improves the prediction of the relative WSS distribution. From the synthetic aneurysmal flow data, PG-VGC recovered the high WSS regions absent in the Spline and Vgrads results, as shown in Fig. 6b. PG-VGC also predicted additional high WSS regions for the *in vivo* BT aneurysm data that were absent in results computed with the other methods as shown in Fig. 8c, thus obtaining WSS distribution more consistent with the CFD results shown (Fig. 6b). Based on *in vivo* aortic 4D flow data, PG-VGC predicted high WSS in regions corresponding to near the VSs, which is consistent with the previous finding that high WSS correlates with VSs in the aorta.[3] The Spline and Vgrads methods failed to predict several of these high WSS regions, as highlighted in Fig. 10. The improved prediction of relative WSS distribution by PG-VGC is valuable for detecting regions with abnormal WSS, as these are related to cardiovascular disease progression such as growth and rupture of intracranial and aortic aneurysms.

There are several limitations of the PG-VGC method. First, time-resolved flow data is needed to determine the temporal derivative of velocity for pressure-gradient estimation. The *in vivo* 4D flow data employed in this study had 13–24 timeframes per cycle, which is standard in clinical acquisitions and was shown to be adequate for PG-VGC to enhance the WSS estimation. Additionally, the cycle-to-cycle variation is not considered since 4D flow MRI acquires the phase-averaged velocity measurement. Moreover, the uncertainty on the wall locations can affect the WSS's accuracy. However, this is a limitation for most WSS estimation methods, and PG-VGC is expected to be more robust than the other methods since it should also reduce the velocity-gradient errors caused by the inaccurate wall location. Another limitation of the PG-VGC method is that the gradient operator generated using the RBF-FD method does not account for the small-scale turbulent structures that exists in the aortic flow. This can affect the accuracy of the estimated pressure drop and the shear stress as shown in the work by Corso *et al.*[13] Compared to the other methods, the computational cost by PG-VGC is significantly higher which is another disadvantage. Using a workstation with 16 cores (Intel Xeon CPU E5-2450 v2) at 2.5 GHz, each iteration of PG-VGC takes about 10 to 15 min on the aneurysmal flow data and about 45 to 60 min on the aortic flow data. The computational time of Spline is about 2 to 3 and 4 to 6 min on the aneurysmal data and the aortic data, respectively. The Vgrads uses about 10 s for the aneurysmal data and 0.5 to 1 min for the aortic data. The M1 and M2 methods spend less than 10 s on processing the aortic flow data.

There are several additional limitations in this study. First, the "ground truth" WSS was unavailable for assessing the WSS errors for the *in vivo* 4D flow data. Moreover, Newtonian flow was assumed for the WSS calculations and the CFD simulations, which may not be ideal in low WSS regions. Additionally, rigid walls were assumed for the cerebral aneurysms and the aorta. Although the rigid wall assumption is reasonable for modeling the flow in cerebral arteries as cine MR images showed no appreciable movements of these vessels over the cardiac cycle in a previous investigation,[6] it may not be appropriate for the aortic wall. However, this limitation should not affect the comparison between different WSS estimation methods.

In conclusion, this study introduced a novel WSS estimation method for 4D flow MRI. The method uses the pressure gradient estimated from the flow data in the whole ROI and flow physics constraints to correct the velocity gradient, therefore enhancing the WSS estimation. The method's performance was evaluated using synthetic and *in vivo* 4D flow data in cerebral aneurysms and thoracic aortas. The proposed method showed reliable estimation of the mean and the relative distribution of WSS with as much as 100% improvement in WSS accuracy. The method can benefit clinical applications of 4D flow MRI as it improves the accuracy of the WSS estimation.

CONFLICT OF INTEREST

The authors have no conflict of interest to report.

REFERENCES

[1]Barker, A. J., C. Lanning, and R. Shandas. Quantification of hemodynamic wall shear stress in patients with bicuspid aortic valve using phase-contrast MRI. *Ann. Biomed. Eng.* 38:788–800, 2010.

[2]Barker, A. J., M. Markl, J. Bürk, R. Lorenz, J. Bock, S. Bauer, J. Schulz-Menger, and F. Von Knobelsdorff-Brenkenhoff. Bicuspid aortic valve is associated with altered wall shear stress in the ascending aorta. *Circ. Cardiovasc. Imaging.* 5:457–466, 2012.

[3]Biasetti, J., F. Hussain, and T. C. Gasser. Blood flow and coherent vortices in the normal and aneurysmatic aortas: a fluid dynamical approach to intra-luminal thrombus formation. *J. R. Soc. Interface.* 8:1449–1461, 2011.

[4]Bieging, E. T., A. Frydrychowicz, A. Wentland, B. R. Landgraf, K. M. Johnson, O. Wieben, and C. J. François. In vivo three-dimensional MR wall shear stress estimation in ascending aortic dilatation. *J. Magn. Reson. Imaging.* 33:589–597, 2011.

[5]Boussel, L., V. Rayz, A. Martin, G. Acevedo-Bolton, M. T. Lawton, R. Higashida, W. S. Smith, W. L. Young, and D. Saloner. Phase-Contrast MRI measurements in intracranial aneurysms in vivo of flow patterns, velocity fields and wall shear stress: a comparison with CFD. *Magn. Reson. Med.* 61:409–417, 2009.

[6]Boussel, L., V. Rayz, C. McCulloch, A. Martin, G. Acevedo-Bolton, M. Lawton, R. Higashida, W. S. Smith, W. L. Young, and D. Saloner. Aneurysm growth occurs at region of low wall shear stress: patient-specific correlation of hemodynamics and growth in a longitudinal study. *Stroke.* 39:2997–3002, 2008.

[7]Brindise, M. C., S. Rothenberger, B. Dickerhoff, S. Schnell, M. Markl, D. Saloner, V. L. Rayz, and P. P. Vlachos. Multi-modality cerebral aneurysm haemodynamic analysis: in vivo 4D flow MRI, in vitro volumetric particle velocimetry and in silico computational fluid dynamics. *J. R. Soc. Interface.* 16:20190465, 2019.

[8]Busch, J., D. Giese, L. Wissmann, and S. Kozerke. Reconstruction of divergence-free velocity fields from cine 3D phase-contrast flow measurements. *Magn. Reson. Med.* 69:200–210, 2013.

[9]Castro, M. A., C. M. Putman, M. J. Sheridan, and J. R. Cebral. Hemodynamic patterns of anterior communicating artery aneurysms: a possible association with rupture. *Am. J. Neuroradiol.* 30:297–302, 2009.

[10]Cecchi, E., C. Giglioli, S. Valente, C. Lazzeri, G. F. Gensini, R. Abbate, and L. Mannini. Role of hemodynamic shear stress in cardiovascular disease. *Atherosclerosis.* 214:249–256, 2011.

[11]Chiu, J. J., and S. Chien. Effects of disturbed flow on vascular endothelium: pathophysiological basis and clinical perspectives. *Physiol. Rev.* 91:327–387, 2011.

[12]Cibis, M., W. V. Potters, F. J. Gijsen, H. Marquering, P. Van Ooij, E. Van Bavel, J. J. Wentzel, and A. J. Nederveen. The effect of spatial and temporal resolution of cine phase contrast MRI on wall shear stress and oscillatory shear index assessment. *PLoS ONE.* 11:1–15, 2016.

[13]Corso, P., G. Giannakopoulos, U. Gulan, C. E. Frouzakis, and M. Holzner. A novel estimation approach of pressure gradient and haemodynamic stresses as indicators of pathological aortic flow using subvoxel modelling. *IEEE Trans. Biomed. Eng.* 68:980–991, 2021.

[14]Corso, P., J. Walheim, H. Dillinger, G. Giannakopoulos, U. Gülan, C. E. Frouzakis, S. Kozerke, and M. Holzner. Toward an accurate estimation of wall shear stress from 4D flow magnetic resonance downstream of a severe stenosis. *Magn. Reson. Med.* 86:1531–1543, 2021.

[15]Cunningham, K. S., and A. I. Gotlieb. The role of shear stress in the pathogenesis of atherosclerosis. *Lab. Investig.* 85:9–23, 2005.

[16]Frydrychowicz, A., A. F. Stalder, M. F. Russe, J. Bock, S. Bauer, A. Harloff, A. Berger, M. Langer, J. Hennig, and M. Markl. Three-dimensional analysis of segmental wall shear stress in the aorta by flow-sensitive four-dimensional-MRI. *J. Magn. Reson. Imaging.* 30:77–84, 2009.

[17]Groen, H. C., F. J. H. Gijsen, A. Van Der Lugt, M. S. Ferguson, T. S. Hatsukami, A. F. W. Van Der Steen, C. Yuan, and J. J. Wentzel. Plaque rupture in the carotid artery is localized at the high shear stress region: a case report. *Stroke.* 38:2379–2381, 2007.

[18]Hunt, J. C. R., A. A. Wray, and P. Moin. Eddies, streams, and convergence zones in turbulent flows. In: Proceedings of the 1988 Summer Program, 1998.

[19]Javed, A., K. Djijdeli, and J. T. Xing. Shape adaptive RBF-FD implicit scheme for incompressible viscous Navier-Strokes equations. *Comput. Fluids.* 89:38–52, 2014.

[20]Jeon, Y. J., G. Gomit, T. Earl, L. Chatellier, and L. David. Sequential least-square reconstruction of instantaneous pressure field around a body from TR-PIV. *Exp. Fluids.* 59:27, 2018.

[21]Jou, L.-D., D. H. Lee, H. Morsi, and M. E. Mawad. Wall shear stress on ruptured and unruptured intracranial aneurysms at the internal carotid artery. *Am. J. Neuroradiol.* 29:1761–1767, 2008.

[22]Leuprecht, A., S. Kozerke, P. Boesiger, and K. Perktold. Blood flow in the human ascending aorta: a combined MRI and CFD study. *J. Eng. Math.* 47:387–404, 2003.

[23]Loecher, M., S. Kecskemeti, P. Turski, and O. Wieben. Comparison of divergence-free algorithms for 3D MRI with three-directional velocity encoding. *J. Cardiovasc. Magn. Reson.* 14:W64, 2012.

[24]Malek, A. M., S. L. Alper, and S. Izumo. Hemodynamic shear stress and its role in atherosclerosis adel. *J. Am. Med. Assoc.* 282:2035–2042, 1999.

[25]Markl, M., S. M. Brendecke, J. Simon, A. J. Barker, C. Weiller, and A. Harloff. Co-registration of the distribution of wall shear stress and 140 complex plaques of the aorta. *Magn. Reson. Imaging.* 31:1156–1162, 2013.

[26]Markl, M., A. Frydrychowicz, S. Kozerke, M. Hope, and O. Wieben. 4D flow MRI. *J. Magn. Reson. Imaging.* 36:1015–1036, 2012.

[27]Meng, H., V. M. Tutino, J. Xiang, and A. Siddiqui. High WSS or low WSS? Complex interactions of hemodynamics with intracranial aneurysm initiation, growth, and rupture: toward a unifying hypothesis. *Am. J. Neuroradiol.* 35:1254–1262, 2014.

[28]Ong, F., M. Uecker, U. Tariq, A. Hsiao, M. T. Alley, S. S. Vasanawala, and M. Lustig. Robust 4D flow denoising using divergence-free wavelet transform. *Magn. Reson. Med.* 73:828–842, 2015.

[29]Paige, C. C., and M. A. Saunders. LSQR: an algorithm for sparse linear equations and sparse least squares. *ACM Trans. Math. Softw.* 8:43–71, 1982.

[30]Paige, C. C., and M. A. Saunders. Algorithm 583: LSQR: sparse linear equations and least squares problems. *ACM Trans. Math. Softw.* 8:195–209, 1982.

[31]Perinajová, R., J. F. Juffermans, J. L. Mercado, J. P. Aben, L. Ledoux, J. J. M. Westenberg, H. J. Lamb, and S. Kenjereš. Assessment of turbulent blood flow and wall shear stress in aortic coarctation using image-based simulations. *Biomed. Eng. Online.* 20:1–20, 2021.

[32]Perinajová, R., J. F. Juffermans, J. J. M. Westenberg, R. L. F. van der Palen, P. J. van den Boogaard, H. J. Lamb, and S. Kenjereš. Geometrically induced wall shear stress vari-

ability in CFD–MRI coupled simulations of blood flow in the thoracic aortas. *Comput. Biol. Med.* 133:104385, 2021.

[33]Potters, W. V., P. Van Ooij, H. Marquering, E. VanBavel, and A. J. Nederveen. Volumetric arterial wall shear stress calculation based on cine phase contrast MRI. *J. Magn. Reson. Imaging.* 41:505–516, 2015.

[34]Rinaudo, A., and S. Pasta. Regional variation of wall shear stress in ascending thoracic aortic aneurysms. *Proc. Inst. Mech. Eng. H.* 228:627–638, 2014.

[35]Rothenberger, S. M., J. Zhang, M. C. Brindise, S. Schnell, M. Markl, P. P. Vlachos, and V. L. Rayz. Modeling bias error in 4D flow MRI velocity measurements. *IEEE Trans. Med. Imaging.* xx:1, 2022.

[36]Santelli, C., M. Loecher, J. Busch, O. Wieben, T. Schaeffter, and S. Kozerke. Accelerating 4D flow MRI by exploiting vector field divergence regularization. *Magn. Reson. Med.* 75:115–125, 2016.

[37]Saunders, M. A. Solution of sparse rectangular systems using LSQR and CRAIG. *BIT Numer. Math.* 35:588–604, 1995.

[38]Sereno, M. F., B. Köhler, and B. Preim. Comparison of divergence-free filters for cardiac 4D PC-MRI data. *Inform. aktuell.* 2018. https://doi.org/10.1007/978-3-662-56537-7_4 4.

[39]Stalder, A. F., M. F. Russe, A. Frydrychowicz, J. Bock, J. Hennig, and M. Markl. Quantitative 2D and 3D phase contrast MRI: optimized analysis of blood flow and vessel wall parameters. *Magn. Reson. Med.* 60:1218–1231, 2008.

[40]Stankovic, Z., B. D. Allen, J. Garcia, K. B. Jarvis, and M. Markl. 4D flow imaging with MRI. *Cardiovasc. Diagn. Ther.* 4:173–192, 2014.

[41]Szajer, J., and K. Ho-Shon. A comparison of 4D flow MRI-derived wall shear stress with computational fluid dynamics methods for intracranial aneurysms and carotid bifurcations—a review. *Magn. Reson. Imaging.* 48:62–69, 2018.

[42]Van Ooij, P., W. V. Potters, J. Collins, M. Carr, J. Carr, S. C. Malaisrie, P. W. M. Fedak, P. M. McCarthy, M. Markl, and A. J. Barker. Characterization of abnormal wall shear stress using 4D flow MRI in human bicuspid aortopathy. *Ann. Biomed. Eng.* 43:1385–1397, 2015.

[43]Van Ooij, P., W. V. Potters, A. Guédon, J. J. Schneiders, H. A. Marquering, C. B. Majoie, E. Vanbavel, and A. J. Nederveen. Wall shear stress estimated with phase contrast MRI in an in vitro and in vivo intracranial aneurysm. *J. Magn. Reson. Imaging.* 38:876–884, 2013.

[44]Wolf, R. L., R. L. Ehman, S. J. Riederer, and P. J. Rossman. Analysis of systematic and random error in MR volumetric flow measurements. *Magn. Reson. Med.* 30:82–91, 1993.

[45]Wright, G. B., and B. Fornberg. Scattered node compact finite difference-type formulas generated from radial basis functions. *J. Comput. Phys.* 212:99–123, 2006.

[46]Zhang, J., M. C. Brindise, S. Rothenberger, S. Schnell, M. Markl, D. Saloner, V. L. Rayz, and P. P. Vlachos. 4D flow MRI pressure estimation using velocity measurement-error-based weighted least-squares. *IEEE Trans. Med. Imaging.* 39:1668–1680, 2020.

[47]Zhou, X., V. Papadopoulou, C. H. Leow, P. Vincent, and M. X. Tang. 3-D flow reconstruction using divergence-free interpolation of multiple 2-D contrast-enhanced ultrasound particle imaging velocimetry measurements. *Ultrasound Med. Biol.* 45:795–810, 2019.

BMES BIOMEDICAL ENGINEERING SOCIETY